Neurobiology of Disease

Homeostatic Dysregulation in Membrane Properties of Masticatory Motoneurons Compared with Oculomotor Neurons in a Mouse Model for Amyotrophic Lateral Sclerosis

Sharmila Venugopal,[1] Chie-Fang Hsiao,[1] Takuma Sonoda,[1] Martina Wiedau-Pazos,[2] and Scott H. Chandler[1]

[1]Departments of Integrative Biology and Physiology, and [2]Neurology, David Geffen School of Medicine, University of California at Los Angeles, Los Angeles, California 90095

Amyotrophic lateral sclerosis (ALS) is a progressive neurodegenerative motoneuron disease with presently no cure. Motoneuron (MN) hyperexcitability is commonly observed in ALS and is suggested to be a precursor for excitotoxic cell death. However, it is unknown whether hyperexcitability also occurs in MNs that are resistant to degeneration. Second, it is unclear whether all the MNs within homogeneous motor pools would present similar susceptibility to excitability changes since high-threshold MNs innervating fast fatigable muscle fibers selectively degenerate compared with low-threshold MNs innervating fatigue resistant slow muscle fibers. Therefore, we concurrently examined the excitability of ALS-vulnerable trigeminal motoneurons (TMNs) controlling jaw musculature and ALS-resistant oculomotor neurons (OMNs) controlling eye musculature in a well studied SOD1 ^{G93A} ALS mouse model using *in vitro* patch-clamp electrophysiology at presymptomatic ages P8–P12. Our results show that hyperexcitability is not a global change among all the MNs, although mutant SOD1 is ubiquitously expressed. Instead, complex changes occur in ALS-vulnerable TMNs based on motor unit type and discharge characteristics. Firing threshold decreases among high-threshold TMNs and increases in a subpopulation of low-threshold TMNs. The latter group was identified based on their linear frequency–current responses to triangular ramp current injections. Such complex changes in MN recruitment were absent in ALS-resistant OMNs. We simulated the observed complex changes in TMN excitability using a computer-based jaw closer motor pool model. Model results suggest that hypoexcitability may indeed represent emerging disease symptomology that causes resistance in muscle force initiation. Identifying the cellular and molecular properties of these hypoexcitable cells may guide effective therapeutic strategies in ALS.

Key words: **brainstem; excitability; mastication; neurodegeneration; presymtomatic**

Introduction

Amyotrophic lateral sclerosis (ALS) is a devastating disease involving degeneration of brain and spinal MNs leading to muscle atrophy, paralysis, and death (Bruijn et al., 2004). Transgenic mouse models of the human neurodegenerative motoneuron disease, ALS mimic the progressive loss of motoneurons (MNs) and allow investigation of mechanisms underlying disease vulnerability. Motoneuron axons die-back causing muscle denervation and loss of functional motor units before MN loss and overt symptoms (Kanning et al., 2010). Moreover, motor axons of fast fatigable (FF) MUs are the first to retract presymptomatically followed by the fast-fatigue resistant (FR) MUs, whereas the slow (S) MUs are spared until the end stage (Pun et al., 2006). Motoneurons forming the FF MUs typically are larger cells with higher recruitment threshold and lower-input resistance than the fatigue resistant (FR and S) MUs (Kernell, 1966; Burke, 1981). This well known "size principle" is fundamental to the "recruitment order" of motor units of a muscle wherein smaller, low-threshold MUs are recruited first followed by larger higher-threshold MUs resulting in increasing muscle force (Enoka and Pearson, 2013). The observed differential MU (Hegedus et al., 2007) and axonal vulnerability (Pun et al., 2006) in ALS raises the possibility of differential abnormalities in MNs forming fast versus slow MUs. Although membrane hyperexcitability has been reported among prototypical MNs (Pieri et al., 2003; Kuo et al., 2004; Durand et al., 2006; van Zundert et al., 2008; Quinlan et al., 2011), whether this occurs regardless of motor unit size is unknown. Concomitant with the preferential loss of fast MUs, an activity-dependent conversion to fatigue resistant MUs occurs that may increase resilience and survival (Hegedus et al., 2008; Gordon et al., 2010). It is unknown whether compensatory changes occur in MN excitability, and if so, how this would alter muscle function. Additionally, a motor pool can consist of MNs with heterogeneous discharge properties (Cotel et al., 2009) that are altered in various diseases (Bennett et al., 2001b; Bories et al.,

Received April 25, 2014; revised Oct. 12, 2014; accepted Oct. 17, 2014.

Author contributions: S.V. and S.H.C. designed research; S.V. and C.-F.H. performed research; M.W.-P. contributed unpublished reagents/analytic tools; S.V., C.-F.H., T.S., and S.H.C. analyzed data; S.V. and S.H.C. wrote the paper.

This work was supported by Grant NS071348 to S.H.C. We thank Dr Dwayne Simmons' laboratory for the confocal imaging facility, and Kelly Lucchesi for assisting with mouse genotyping.

The authors declare no competing financial interests.

Correspondence should be addressed to Dr Scott H. Chandler, UCLA, 2859 Slichter Hall, 603 Charles East Young Drive East, Los Angeles, CA 90095-7246. E-mail: schandler@physci.ucla.edu.

DOI:10.1523/JNEUROSCI.1682-14.2015

 0270-6474/15/350707-14$15.00/0

2007). Therefore, we hypothesized that ALS vulnerable MNs show presymptomatic abnormalities in membrane properties that may be selective to MU type and MN discharge characteristics.

Second, it is unknown whether the ubiquitous expression of mutant SOD1 alters MN excitability in disease resistant motor nuclei, such as the brainstem oculomotor neurons. The oculomotor neurons (OMNs) and the related oculomotor functions are relatively spared in ALS patients (Radcliffe and Lockhart Clarke, 1862) and in mouse models of the disease (Nimchinsky et al., 2000; Angenstein et al., 2004; Niessen et al., 2006). In contrast, the closely located brainstem trigeminal motoneurons controlling jaw movements are vulnerable to degeneration (Angenstein et al., 2004; Niessen et al., 2006; Ferrucci et al., 2010) and the related masticatory functions are compromised to varying degrees in ALS (Brooks, 1996). The mechanisms underlying the early changes in neuronal excitability, whether causative or adaptive, are not clear. Early homeostatic and compensatory regulation for neuroprotection of the motor pool undoubtedly masks early disease deficits (Saxena et al., 2013). Here we focus on the early adaptive changes in excitability in ALS-vulnerable trigeminal motoneurons (TMNs) and ALS-resistant OMNs in a postnatal (P8–P12) SOD1^{G93A} ALS mouse model (Gurney et al., 1994) to gain insight into the mechanisms underlying disease progression and the basis for differential vulnerability of neuron types.

Materials and Methods

Transgenic mice overexpressing the human SOD1^{G93A} transgene and their WT littermates were used for this study. Experiments were performed on postnatal 8- to 12-d-old mice of either sex. Data presented are from 113 motoneurons with 60 cells from 42 WT animals and 53 cells from 38 age-matched SOD1^{G93A} high expressor mutant animals. All animal protocols were approved by the Institutional Animal Care and Use Committee at UCLA.

Motoneuron identification. The trigeminal motor nucleus was identified in coronal brainstem slices in bright field as an opaque, pale oval region that is medial to the trigeminal principal sensory nucleus and ventrolateral to the periaqueductal gray (Chandler et al., 1994). Of the 75 TMNs presented in this study, 46 were labeled with a red fluorescent dye (AlexaFluor 568 hydrazide) injected from the pipette during patch-clamp recording for *post hoc* imaging and location analyses. In some instances (26/75 cells), the TMNs were identified in retrogradely labeled motor trigeminal nucleus (Mot V) by injecting a green fluorescent retrograde tracer (AlexaFluor 488 hydrazide)

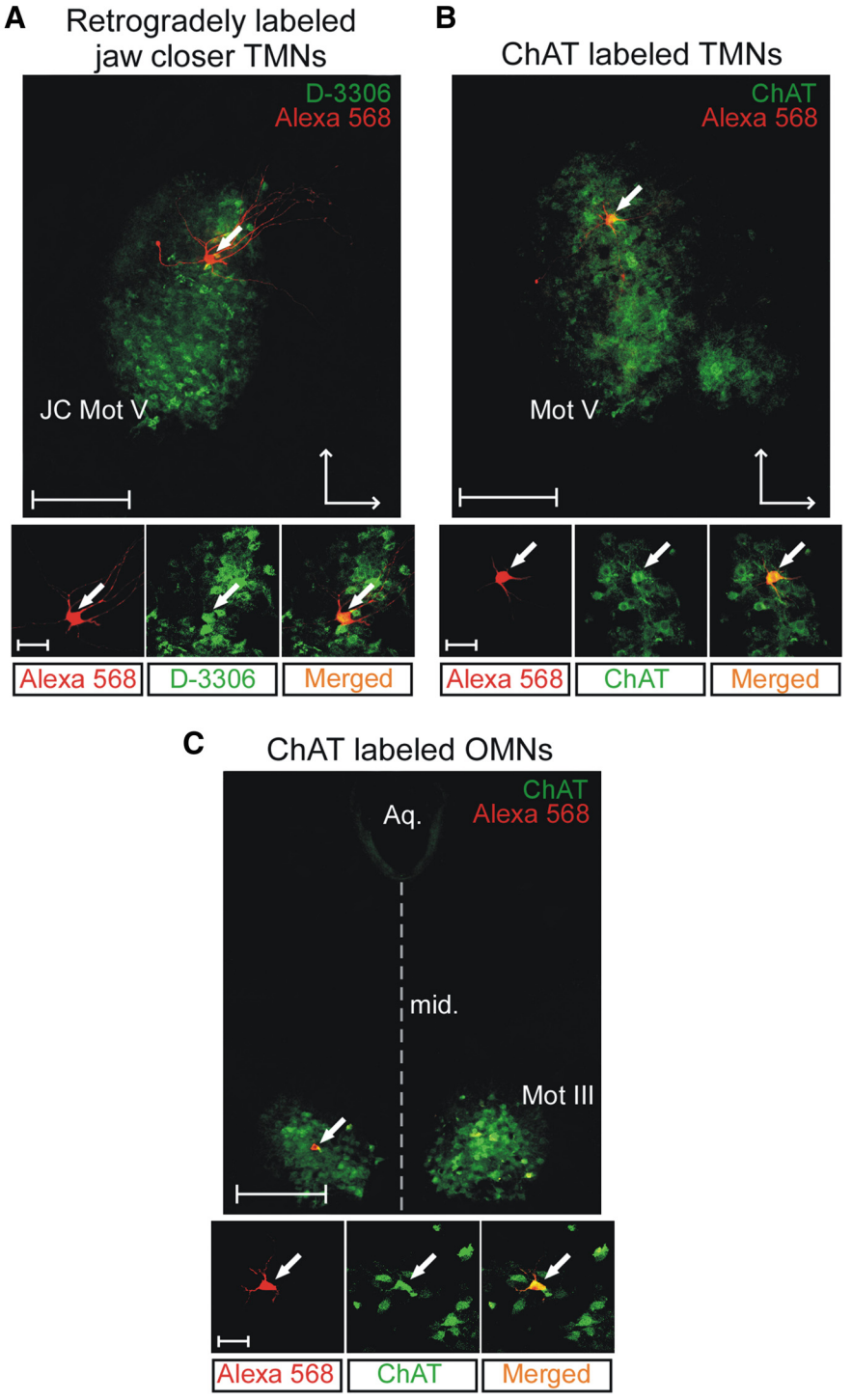

Figure 1. Identification of trigeminal and oculomotor motoneurons. ***A***, Top, Trigeminal motor nucleus labeled by retrograde tracer injection into JC muscles; D-3306: green fluorescent dextran injected into the JC muscles shows labeled cell bodies of JC TMNs; AlexaFluor 568: red fluorescent dye filled single motoneuron. Bottom, High-magnification image of the double-labeled JC TMN with D-3306 and AlexaFluor 568. ***B***, Top, Trigeminal motor nucleus (Mot V) immunolabeled for ChAT using AlexaFluor 488 (green). The ventromedial cell group is also seen; Alexa Fluor 568: red fluorescent dye placed in the patch pipette filled the MN during patch-clamp recording, in turn double-labeling the TMN in the dorsolateral aspect of the Mot V where jaw closers are present. Bottom, High-magnification image of the double-labeled TMNs with AlexaFluor 488 (ChAT) and AlexaFluor 568 in the cell. ***C***, Top, Oculomotor nucleus bilaterally identified by ChAT immunohistochemistry using AlexaFluor 488 (green). AlexaFluor 568 fill of a ChAT-positive OMN (red). Aq, Cerebral aqueduct; mid, midline. Bottom, High-magnification image of the double-labeled OMN with AlexaFluor 488 (ChAT) and AlexaFluor 568 in the cell. Scale bars: low-magnification, 200 μm; high-magnificatio, 40 μm. ***A***, ***B***, Horizontal arrows indicate medial and vertical arrows indicate dorsal orientations.

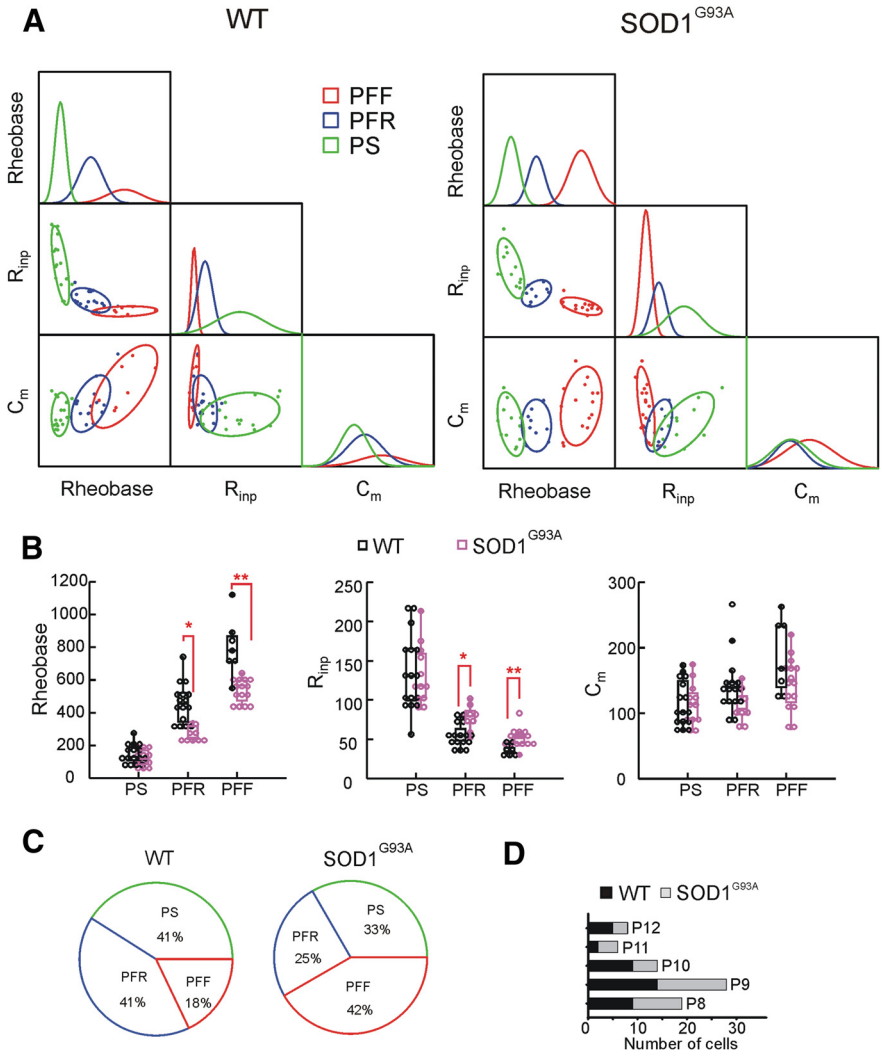

Figure 2. Motor unit classification based on TMN membrane properties. ***A***, Scatterplot matrices of membrane properties including rheobase, R_{inp} and C_m showing the result of *k*-means clustering based classification of motor units with PS in green, PFR in blue, and PFF in red, in both WT (left) and SOD1 ^{G93A} (right) TMNs. The diagonal cells show the normal curves for each MU group. In WT the *F*-ratios were 130.2, 26.4, and 12.9, and in the mutant these values were 163.2, 36.6, and 3.7, respectively, for rheobase, input resistance, and membrane capacitance. ***B***, Comparison of membrane properties of MU groups between WT (black) and SOD1 ^{G93A} (magenta) TMNs. Rheobase values were significantly lower among SOD1 ^{G93A} PFR and PFF units compared with WT (Student's *t* test, $*p = 0.0002$ for PFR, $**p = 0.0001$ for PFF), whereas R_{inp} values were significantly greater (Student's *t* test, $*p = 0.0009$ for PFR, $**p = 0.0028$ for PFF). Error bars indicate SD. ***A***, ***B***, Units of rheobase, R_{inp}, and C_m are pA, MΩ, and pF, respectively. ***C***, Chi-square test of distribution of the three MU types in WT and SOD1 ^{G93A} Mot V yielded significant difference ($p = 0.0014$) for the presented dataset. ***D***, Distribution of cells across the age range considered (P8–P12). Data from 28 WT mice ($n = 39$) and 26 SOD1 ^{G93A} mutant mice ($n = 36$), where *n* is the number of cells.

into the jaw closer (JC) musculature 48–72 h before patch-clamp recording (Fig. 1*A*). Fifteen TMNs with the red dye were identified in the Mot V using *post hoc* confocal imaging of which nine cases were used for double-labeling with choline acetyl transferase (ChAT) with green AlexaFluor 488 hydrazide to further affirm motoneuron identity (Fig. 1*B*). In initial experiments, the location of the oculomotor nucleus (Mot III) was confirmed in the ventrolateral corner of the periaqueductal gray by retrogradely labeling the Mot III by injection of a green retrograde tracer (AlexaFluor 488 hydrazide) into the extraocular musculature 48–72 h before slice preparation. The located Mot III sections were 1 mm rostral from the sections containing the trigeminal motor nucleus. In subsequent experiments without retrograde tracing of the Mot III nucleus, patched OMN location was confirmed by injecting a red fluorescent dye (AlexaFluor 568 hydrazide) into the cell during patch-clamp recording followed by *post hoc* confocal imaging of the cell location in 20/38 cells. In a subset of these cells (5/20), motoneuron identity was further affirmed by double-labeling with ChAT (green AlexaFluor 488 hydrazide) immunohistochemistry (Fig. 1*C*).

Solutions. All solutions were bubbled with 95% O_2/ 5% CO_2 and maintained at pH 7.25–7.3. The brain-cutting solution used during slice preparation was composed of the following (in mM): 126 NaCl, 3 KCl, 1.25 NaH_2PO_4, 26 $NaHCO_3$, 10 glucose, 1 $CaCl_2$, 5 $MgCl_2$, and 4 lactic acid (Del Negro and Chandler, 1998; del Negro et al., 1999), or 85 NaCl, 2.5 KCl, 1.25 NaH_2PO_4, 24 $NaHCO_3$, 25 glucose, 75 sucrose, 0.5 $CaCl_2$, and 4 $MgCl_2$ (Gupta et al., 2012). The slice incubation solution was composed of the following (in mM): 124 NaCl, 3 KCl, 1.25 NaH_2PO_4, 26 $NaHCO_3$, 10 glucose, 2 $CaCl_2$, 2 $MgCl_2$, and 4 lactic acid (Schurr et al., 1988). The external recording solution during patch-clamp recording consisted of the following (in mM): 124 NaCl, 3 KCl, 1.25 NaH_2PO_4, 26 $NaHCO_3$, 10 glucose, 2 $CaCl_2$, and 2 $MgCl_2$. The pipette internal solution used in current-clamp experiments was composed of the following (in mM): 115 K-gluconate, 9 NaCl, 1$MgCl_2$, 10 HEPES buffer, 0.2 EGTA, 3 K2-ATP, and 1 Na-GTP with a pH between 7.28 and 7.3, and osmolarity between 290 ± 5 mOsm.

Slice preparation. P8–P12 mice were anesthetized by inhalation of isofluorane and then decapitated. The brain was then removed and immersed in ice-cold cutting solution. The extracted brain block was mounted on a vibrating slicer (DSK Microslicer, Ted Pella) supported by an agar block. Coronal brainstem sections (250 μm) consisting of Mot V and Mot III were obtained from caudal to rostral order. Slices were then placed into the incubation solution for 40–50 min at room temperature (22–24°C).

Patch-clamp electrophysiology. Patch pipettes (3–5 MΩ) were pulled using a Brown/Flaming P-97 micropipette puller (Sutter Instruments). Slices were perfused with oxygenated recording solution (2 ml/min) while secured in a glass bottom recording chamber mounted on a Zeiss fixed-stage Axioskop microscope. Neurons were visualized with infrared differential video microscopy. Current-clamp recordings were performed with an Axopatch-1D amplifier (Molecular Devices) with pCLAMP acquisition software (v9.2, Medical Devices) with a sampling rate between 20 and 50 kHz. Signals were grounded by a 3M KCl agar bridge electrode mounted in the recording well.

Data analysis and statistics. Data were analyzed using Clampfit v9.2 (Molecular Devices), Sigma-Aldrich Plot v9.0, SYSTAT 13 (Systat Software), StatView (SAS Institute), and Microsoft Excel. Cells with resting membrane potential more negative than −50 mV and action potential height ≥70 mV measured from spike voltage threshold to peak amplitude were included in the dataset. Although interneurons were avoided during patch-clamp recording through selection of visibly large neurons when retrograde tracer was not used, acceptable motoneurons had membrane capacitance >70 and <300 pF and input resistance <200 MΩ in agreement with values noted from our identified motoneuron recordings. One of two protocols was used to measure membrane capacitance: (1) 15 ms hyperpolarizing voltage commands from −70 to −50 mV in 5 mV steps, and, (2) 10 sweeps of 10 ms voltage command from −70 to −50 mV. In both cases, membrane capacitance was calculated as the

average of the integral of capacitive current across the voltage sweeps. Input resistance was determined from the slope of the linear portion of the steady-state *I–V* relationship from a −60 mV holding potential in current-clamp mode. Voltage responses at the end of 1 s hyperpolarizing current pulses were used to obtain the *I–V* relationship. Steady-state mean frequencies in response to 1 s current pulses were obtained by calculating the mean frequency of the last 500 ms of the evoked action potential train. Discharge patterns of cells were classified based on membrane response to triangular ramp current injection of 10 s duration and magnitude between 1.5 and 5 times firing threshold current. Instantaneous firing frequencies were calculated to generate *f–I* curves. The results are reported as mean ± SD, unless stated otherwise. Statistical tests consisted of Student's *t* test, two-way repeated-measures ANOVA and χ^2 proportionality test, and group differences were considered significant if $p < 0.05$.

Motor unit prediction based on MN membrane properties. We predicted motor unit type as slow and fast (fatigable or fatigue resistant) based on membrane properties of motoneurons recorded in this study. Previous studies have demonstrated that mechanically typed spinal MUs can be classified into fast (FF, FR) and slow based on membrane properties, such as rheobase and input resistance of the motoneurons with >90% accuracy (Zengel et al., 1985). Because such measurements are commonly made during patch-clamp recordings, we used predictive *k*-means clustering algorithm (SYSTAT 13) to classify motor unit types based on rheobase, input resistance, and membrane capacitance of motoneurons as categorical variables. The algorithm is based on iterative assignment of a set of observations into *k*-clusters by maximizing between-cluster variation and minimizing within-cluster variation. Squared Euclidean distance from the cluster mean was chosen as the parameter that determines cluster variations. Initial seeds (*k* mean values) were not explicitly specified since the observations were made independent of any associable mechanical properties traditionally used for motor unit typing and hence initial cluster means could not be assumed. Significance of classification was noted by the *F*-ratio (ratio of between group variance and within group variance) for each categorical variable. Larger *F*-ratio denoted better statistical power of the categorical variable in distinguishing the underlying clusters in the dataset.

Immunohistochemistry and confocal imaging. AlexaFluor 568 fluorescent dye in the pipette internal solution filled the cells during whole-cell patch-clamp recording. Slices obtained after recording were placed in a 2% paraformaldehyde PBS solution overnight at 4°C, and then permeabilized in 2% Triton X-100 to increase antibody penetration. Motoneuron identity was confirmed by incubating sections in primary goat antibody against ChAT (1:500). Slices were then incubated in Northern Lights 493 donkey anti-goat secondary antibody (1:200; R&D Systems) and mounted on glass slides (Fisher) using aqueous mounting medium (Daido-Sangyo). Slices were then imaged using a confocal microscope (Zeiss LSM 5) attached to an upright microscope (Zeiss, AxioImager) along with Zen 2008 software (Carl Zeiss MicroImaging). Motoneuron identity was confirmed when the cell that was filled with red dye was double-labeled with green ChAT immunolabeling in the nucleus of interest (Fig. 1). For morphology analyses, *z*-stack images were obtained at high-magnification (63×) with 1 μm depth resolution. Three-dimensional projection of cells were rendered from *z*-stacks using Volocity 3D Image Analysis software (PerkinElmer) and a region-of-interest was manually established to measure soma surface area excluding dendrites.

Genotyping. Mouse genotype as homozygous WT or heterozygous SOD1^{G93A} was determined using standard PCR technique using the DNeasy 96 Blood and Tissue Kit (Qiagen) according to the manufacturer's protocols. Briefly, frozen samples (mouse tails ~0.5 cm) were incubated overnight (16–18 h) in 0.2 ml lysis buffer (80% ATL and 20% proteinase K, DNeasy Kit) at 56°C. 200 μl AL buffer and 200 μl 100% ethanol were added to the lysate before loading onto the DNeasy Mini Spin Column and centrifuged at 6000 rpm for 1 min to allow selective DNA binding to DNeasy membrane. This was followed by two efficient wash steps to remove remaining contaminants and enzyme inhibitors. The supernatant was incubated in AE buffer for 1 min and then centrifuged. The collected sample was used for PCR. The PCR mix for each sample consisted of 10 μl 2× TAG PCR Master Mix, four primers, 0.5 μl each for PCR amplification, 6 μl of double-distilled water and 2 μl of DNA from sample. PCR amplification used the following primers (5′ to 3′): for the wild-type allele, CTAGGCCACAGAATTGAAAGATCT and GTAGGTGGAAATTCTAGCATCATCC; and for the mutant allele, CATCAGCCCTAATCCATCTGA and CGCGACTAACAATCAAAG TGA (Integrated DNA Technologies). The reaction consisted of 3 min at 94°C, 35 cycles of 30 s at 95°, 30 s at 60°C, 45 s at 72°C, and 2 min at 72°C. PCR products were separated on a 1.5% agarose gel, allowing resolution of a 324 bp product for the WT allele and a 236 bp product for the mutant allele.

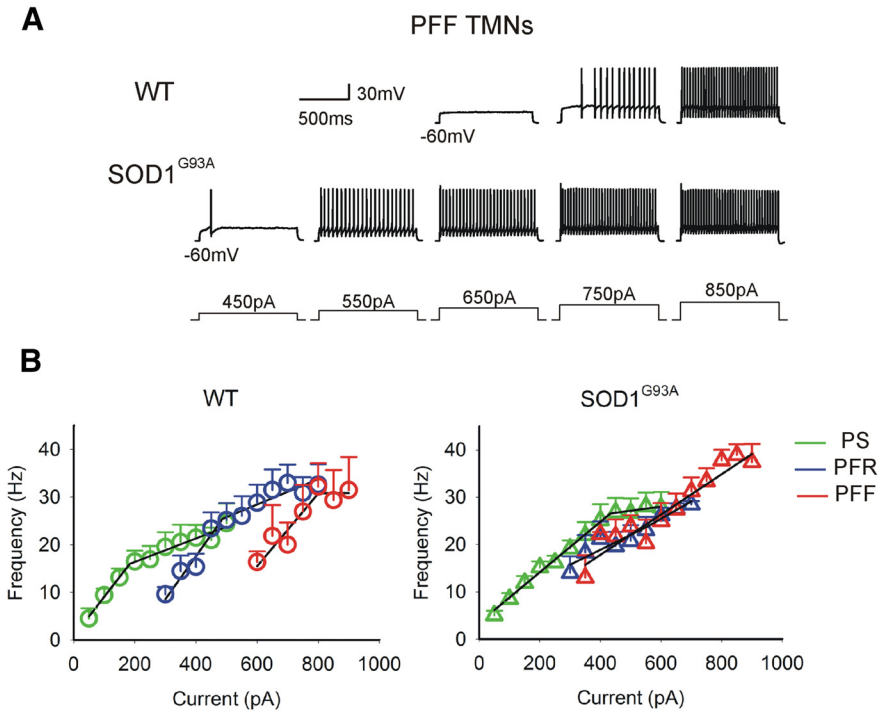

Figure 3. Frequency–current responses in the predicted TMN motor units. ***A***, Membrane voltage responses to increasing levels of 1 s current injection (bottom traces); top and bottom traces show example PFF TMNs from WT and SOD1^{G93A} mice respectively. ***B***, Average steady-state frequency–current responses in WT (circles) and SOD1^{G93A} (triangles) TMNs. The PS, PFR, and PFF cells are depicted in green, blue, and red, respectively. Error bars indicate SEM and black lines indicate linear fits to TMN frequency range(s).

Motor pool simulation model. Identifying a single motor pool using retrograde tracer injection is technically challenging in neonates. Nonetheless, our retrograde tracer injection targeted musculature visibly located on either sides of the jaw laterally in the mandibular region (thus excluding jaw openers) that labeled one or more JC motor pools: masseter, temporalis, and pterygoid. All the *post hoc* identified TMNs were in the lateral aspect of the Mot V corresponding to the dorsolateral subdivisions of the trigeminal motor nucleus consisting of JC motor pools (Limwongse and DeSantis, 1977; Matsuda et al., 1978; Uemura-Sumi et al., 1982). Therefore, we assumed a motor pool consisting of JC MNs for our model simulation. Classical studies suggest that based on the muscle fiber type composition, all the jaw closer muscles are considered fast muscles (Taylor et al., 1973). Particularly in the rat (Hiiemae, 1971), as well as in the mouse (Gojo et al., 2002), ~70% of the fibers types in all of the above three jaw closer muscles are FF, whereas the remaining

Table 1. Membrane properties of WT and SOD1 ^{G93A} TMNs classified by predicted MU type

	PS		PFR		PFF	
Membrane property	WT ($n = 16$)	SOD1 ^{G93A} ($n = 12$)	WT ($n = 16$)	SOD1 ^{G93A} ($n = 9$)	WT ($n = 16$)	SOD1 ^{G93A} ($n = 15$)
C_m, pF	115.0 ± 8.4	114.0 ± 7.8	142.2 ± 11.0	111.7 ± 8.3	185.6 ± 21.2	144.7 ± 10.5
R_{inp}, MΩ	132.8 ± 12.8	131.7 ± 8.4	59.1 ± 3.9	**78.6 ± 5.3***	35.7 ± 2.2	**51.4 ± 3.0****
RMP, mV	−61.6 ± 1.8	−60.1 ± 1.6	−65.5 ± 1.2	−65.9 ± 2.4	−67.4 ± 1.6	−64.4 ± 1.5
Rheobase, pA	151.6 ± 13.8	123.8 ± 13.8	459.1 ± 30.2	**274.4 ± 16.5†**	800.7 ± 67.3	**539.3 ± 19.1††**
AP threshold, mV	−40.0 ± 1.3	−39.4 ± 1.2	−33.5 ± 1.3	−36.5 ± 2.6	−33.5 ± 2.3	−31.2 ± 1.3
AP height, mV	83.5 ± 2.8	85.7 ± 2.8	79.1 ± 2.2	83.3 ± 3.7	82.1 ± 2.6	**73.8 ± 1.5‡**
AP half-width, ms	1.0 ± 0.05	0.9 ± 0.1	0.8 ± 0.04	**1.0 ± 0.1#**	0.7 ± 0.07	0.8 ± 0.0
AHP, mV	−5.4 ± 1.3	−3.8 ± 1.1	−4.0 ± 1.1	−5.4 ± 1.5	−3.4 ± 1.1	−3.4 ± 0.7

Values reported as mean ± SEM. Student *t* tests were performed for statistical comparison between WT and SOD1 ^{G93A} neurons within the three predicted MU types. Symbols indicate statistical significance, where: $*p = 0.007$, $**p = 0.003$, $†p = 0.00024$, $††p = 7.83712E\text{-}05$, $‡p = 0.0074$, $\#p = 0.032$. Bold face highlights values that show statistical significance in the mutant.

(~30%) represent slow-twitch and FR types. Hence, we assumed a motor pool consisting of 100 MNs of which 70 were MNs corresponding to fast MUs and 30 were MNs corresponding to slow MUs. Each MN was represented by three sets of intrinsic properties: (1) the steady-state frequency–current (*f–I*) gain functions G_1 (gain in the primary range) and G_2 (gain in the secondary range; Granit et al., 1966), (2) threshold currents for recruitment (I_{thresh}) and primary-to-secondary range transition current (I_{trans}), and (3) recruitment frequency (f_{thresh}) and transition frequency from G_1 to G_2 (f_{thresh}). All of these values were derived from our present data. Table 3 shows the distribution of these properties for the entire motor pool along with the assumed properties of the muscle. The two main sets of MN properties that were explicitly altered to simulate abnormalities in SOD1 ^{G93A} TMNs include the cells' recruitment threshold (I_{thresh}), and *f–I* gain values (G_1 and G_2). Changes in I_{thresh} in turn altered I_{trans} as given by the following equation:

$$I_{trans} = I_{thresh} + \left(\frac{f_{trans} - f_{thresh}}{G_1}\right)$$

(see Results).

The isometric MU force–frequency transformation was performed as by Heckman and Binder (1991) based on the following equation:

$$F = F_{max}\left(1 - e^{\left(\left(\frac{f}{T_f}\right)^P\right)}\right).$$

F_{max} is the maximal tetanic force of the MU, and its range across the 100 MUs was based on the range of isometric contraction forces achieved at the optimal jaw muscle length reported in rabbit masseter muscle units (Turkawski and van Eijden, 2000; van Eijden and Turkawski, 2002) due to lack of more specific data from mice. T_f is a frequency constant related to the speed of contraction of the muscle unit and was estimated using the following equation:

$$T_f = \frac{f_{thresh}}{(0.0834)^P},$$

where

$$P = \frac{1}{Log_{19.3}\left(\frac{f_{trans}}{f_{thresh}}\right)},$$

a factor that transforms an exponential to sigmoid function. The above MU force–frequency functions were based on the percentages of maximal force output actually generated by motor units at f_{thresh} and f_{trans}, assuming nearly 8% of F_{max} is generated at f_{thresh} and 80% of F_{max} is generated at f_{trans} (i.e., at the end of the primary range; Kernell, 1979). The steady-state input-output function of the simulated motor pool (i.e., isometric force versus effective MN pool input) is a sigmoidal curve where each value on the curve is a summation of all of the MU forces at that input level (Kernell et al., 1983); i.e.,

$$F_{isometric} = \sum_{i=1}^{100} F_i,$$

where F_i is the isometric MU force obtained above. Note that the properties of muscle fibers were not modeled explicitly and were assumed not to change significantly at this postnatal stage in the mutant mouse. The motor pool model was constructed and simulated using MATLAB (MathWorks).

Results

Prediction of motor unit types and hyperexcitable shifts in SOD1 ^{G93A} TMNs forming fast motor units

Studies based on SOD1 ^{G93A} mice have suggested preferential loss of fast motor units before symptom onset in ALS. Although maturational electrophysiological abnormalities have been demonstrated in motoneurons, such changes have not been associated with motor unit type because measuring mechanical properties of motor units to separate fast versus slow populations in young animals is technically challenging. Therefore, using an advanced statistical clustering approach, here we first predicted motor unit types based on motoneuron membrane properties, and then tested the hypothesis that motoneurons forming fast MUs may present excitability changes that are different from motoneurons forming slow MUs. First, we used *k*-means cluster analyses to predict the major types of motor units: predicted slow (PS), predicted fast fatigue resistant (PFR) and predicted fast fatigable (PFF) using rheobase, input resistance, and membrane capacitance as clustering variables (see Materials and Methods). Figure 2*A* shows the results of *k*-means clustering and the normal curves shown indicate the separation of the three MU populations in both WT and SOD1 ^{G93A} groups. Note that the rheobase and input-resistance of PS, PFR, and PFF TMNs vary in accordance to the expected variation among low-threshold slow MUs and higher threshold fast MUs in both WT and SOD1 ^{G93A} groups. Similarly, membrane capacitance was on average lowest in the PS TMNs and progressively larger in PFR and PFF cells, respectively. Among the clustering variables, rheobase yielded the highest *F*-ratios followed by input resistance and membrane capacitance respectively in both WT and SOD1 ^{G93A} (Fig. 2, legend). Based on this classification, we then compared the membrane properties of WT and SOD1 ^{G93A} TMNs among the predicted MU types. We observed that both PFF and PFR SOD1 ^{G93A} TMNs showed hyperexcitable shifts marked by reduced rheobase and increased input resistance, whereas PS TMNs did not present significant alterations in these properties (Fig. 2*B*). Membrane capacitance that was least effective in MU clustering was not different between WT and SOD1 ^{G93A} motor units of all types. Interestingly, there was a significant difference in the proportions of MU types in the WT and SOD1 ^{G93A} groups (Fig. 2*C*) despite proportionate age distribution in the two animal groups (Fig. 2*D*). Steady-state frequency–current (*f–I*) responses for current injections <600

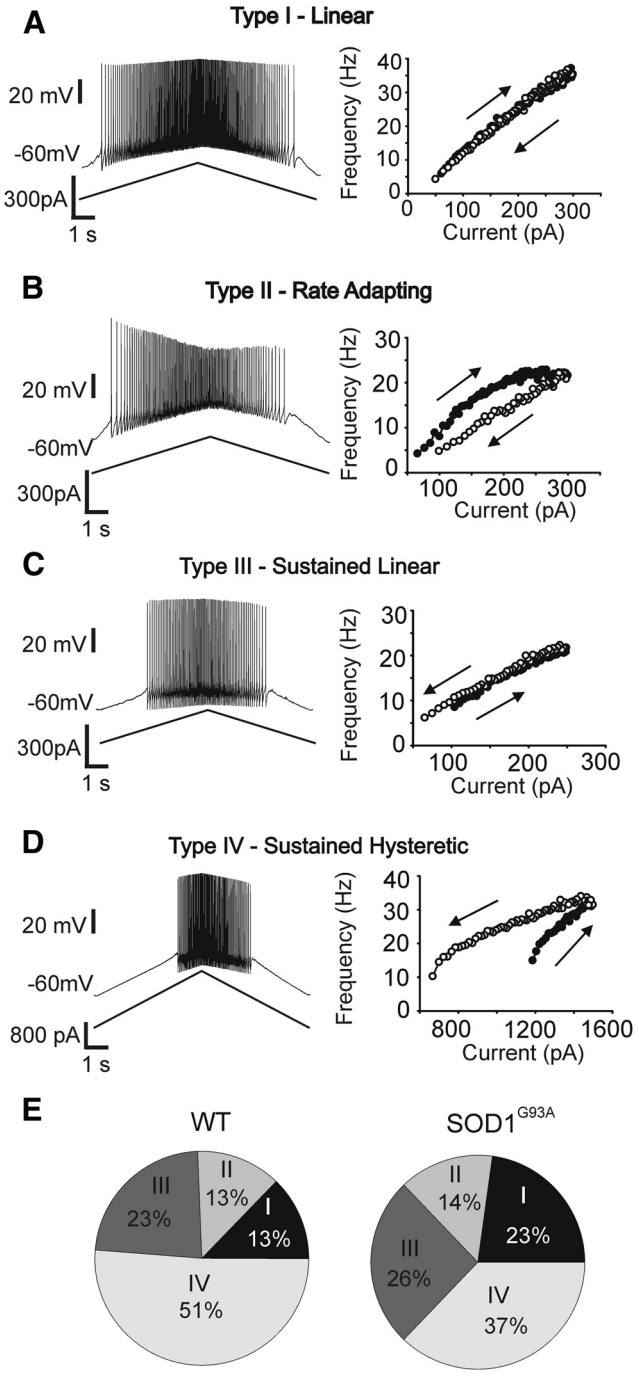

Figure 4. Heterogeneous discharge patterns in TMNs. ***A–D***, Membrane voltage responses (left) of four TMNs to injection of triangular ramp currents (bottom traces) and the corresponding plots of instantaneous discharge frequency responses to ascending and descending current ramps (right) are shown by filled and open circles respectively. Arrows point to the direction of the current ramp. Types I–IV refer to the four types of discharge patterns (see section Discharge patterns of TMNs and their altered distributions in SOD). ***E***, Proportions of the four types of discharge patterns found in WT and SOD1 ^{G93A} TMNs were significantly different (χ^2 test: $p = 0.0007$).

pA showed hyperexcitability in SOD1 ^{G93A} PFF TMNs (Fig. 3) wherein WT PFF TMNs did not respond during these lower current injections during steady-state. Note that this is consistent with reduced firing threshold due to reduced rheobase and increased input resistance (Fig. 2*B*; Table 1). However, for larger current injections >600 pA where PFF TMNs of both genotypes responded, no statistically significant differences existed in the steady-state *f–I* responses between WT and SOD1 ^{G93A} TMNs (two-way repeated-measures ANOVA; Fig. 3). Similarly, the steady-state *f–I* responses were not different among WT and SOD1 ^{G93A} PS and PFR TMNs (two-way repeated-measures ANOVA; Fig. 3*B*). Interestingly, we noted qualitative differences in the overall pattern of *f–I* curve distribution among the three predicted MU types in WT versus SOD1 ^{G93A} recordings. For instance, over the range of injected current tested (Fig. 3*B*), the WT MU groups presented distinct primary range *f–I* curves (lower arm of bilinear fits) as normally expected within a motor pool, whereas the SOD1 ^{G93A} MU group primary range *f–I* curves overlapped particularly for the PFR and PFF TMNs.

Discharge patterns of TMNs and their altered distribution in SOD1 ^{G93A} jaw motor pool

The absence of hyperexcitable shifts among SOD1 ^{G93A} PS TMNs is consistent with our initial hypothesis that MNs forming fast MUs would show selective disease vulnerable modifications, such as hyperexcitability. However, we sought to determine whether more subtle changes in excitability would be revealed if we examined TMN properties according to discharge patterns. To test this possibility, we classified the TMNs based on their discharge properties in response to a somatic injection of triangular ramp current. As described for spinal motoneurons (Bennett et al., 2001a; Button et al., 2006; Cotel et al., 2009), we observed four qualitatively distinct discharge patterns as shown in Figure 4*A–D*.

Type I neurons show a "linear" relationship in the injected current–frequency response with discharge frequencies matched during both ascending and descending current ramps (Fig. 4*A*). Type II neurons show rate adaptation during the descending ramp (Fig. 4*B*). Type III cells show linearity of frequencies during ascending and descending ramps, but with a prominent sustained discharge during the descending ramp that is below the recruitment (or threshold) current (Fig. 4*C*). Type IV cells also show a sustained discharge during descending ramp accompanied by a counter-clockwise hysteresis in the *f–I* relationship (Fig. 4*D*). All four patterns were found among mutant TMNs as well (data not shown). Although in both WT and mutant Mot V, Types III and IV together were the most abundant and the Type II was the least abundant, proportions of cells with these discharge patterns were significantly different in the mutant motor nucleus (χ^2 proportion test: $p = 0.0007$; Fig. 4*E*).

Compensatory changes in TMN excitability in SOD1 ^{G93A} mice according to discharge characteristics

Interestingly, based on the classification according to discharge characteristics, membrane properties were altered among Types I and II, but not in Type III and IV cells in the mutant Mot V compared with WT (Fig. 5*A*). For example, the Type II cells showed a hyperexcitable shift with a significant reduction in rheobase. However, note that such neurons appear to decrease in proportion in the SOD1 ^{G93A} Mot V (Fig. 4*E*). In contrast, the Type I linear cells, that were more abundant in the mutant Mot V (Fig. 4*E*), emerged as a hypoexcitable group with increased rheobase and more depolarized spike voltage threshold (Fig. 5*A*,*B*). On average the steady-state *f–I* response was also lower in mutant Type I TMNs compared with WT but not statistically significant (two-way repeated-measures ANOVA; Fig. 5*C*). This suggests that such decreases in discharge frequencies shown in Figure 5*C* are likely a product of increased firing threshold as observed by rheobase and spike threshold changes. Interestingly, both Type I and Type II cells were distributed among PS type TMNs in the

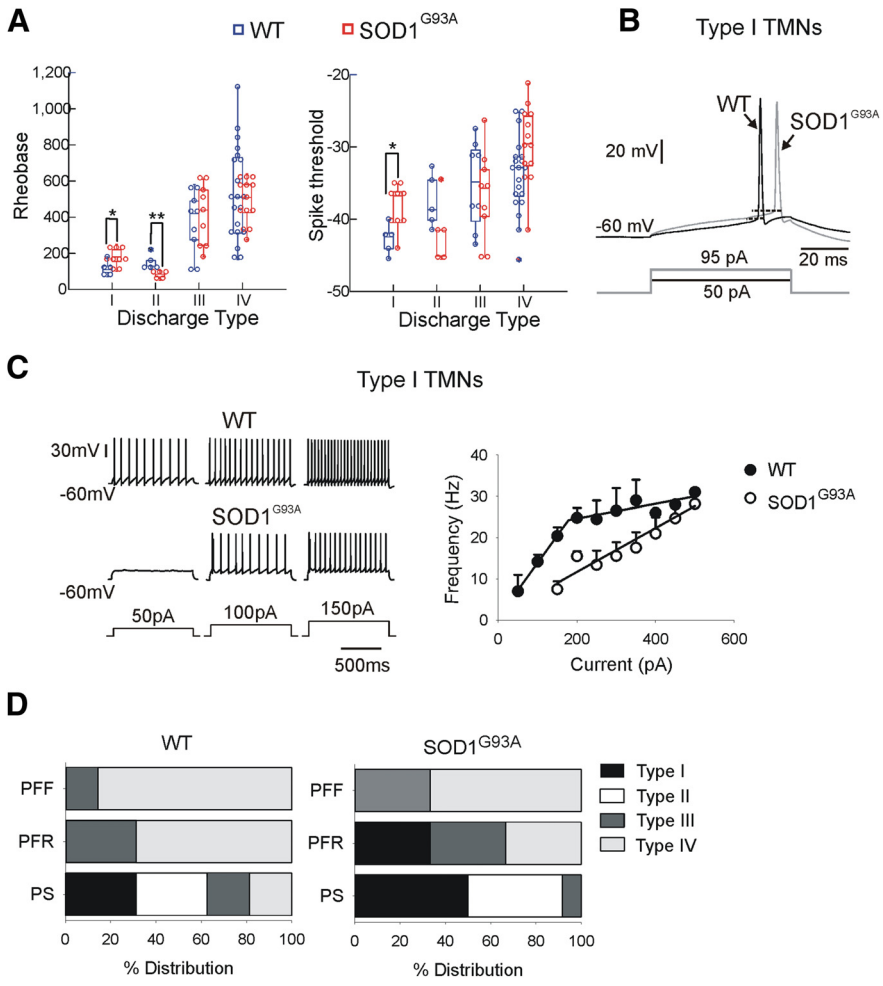

Figure 5. SOD1 ^{G93A} TMNs with Type I linear discharge pattern show unexpected changes in excitability. ***A***, Comparison of membrane properties based on discharge types between WT (blue) and SOD1 ^{G93A} (red) TMNs. Rheobase (left) and voltage threshold for spike (right) showed opposite changes among Type I and II cells. Type I cells showed significant increase in rheobase, whereas Type II TMNs showed significant decrease in rheobase (Student's *t* test, $*p = 0.034$, $**p = 0.0103$). Spike threshold was significantly depolarized in Type I cells (Student's *t* test, $*p = 0.0131$). Units of rheobase and spike threshold are pA and mV, respectively. Error bars indicate SD. ***B***, Examples showing increased rheobase and spike threshold in SOD1 ^{G93A} Type I TMNs compared with WT. ***C***, Left, Membrane voltage responses to increasing levels of 1 s current injection (bottom traces) in WT (top trace) and SOD1 ^{G93A} (middle traces) Type I TMNs. Right, Average steady-state frequency–current responses in WT ($n = 5$ cells from 5 animals) and SOD1 ^{G93A} ($n = 9$ from 8 animals) Type I TMNs. Error bars indicate SEM and black lines indicate linear fits to TMN frequency range(s). ***D***, Distribution of different discharge types among PS, PFR, and PFF TMNs. Bar charts show percentage composition of the four discharge types among the predicted MU types.

WT group, whereas Types III and IV were largely PFR and PFF cells (Fig. 5*D*). However, in the mutant, the proportional increase in the Type I cells (Fig. 4*E*) was partly distributed among PFR TMNs suggesting a possible homeostatic mechanism of excitability compensation in the fast MN group through increases in the proportion of hypoexcitable cells in the jaw motor pools. Concomitantly, the SOD1 ^{G93A} group also showed a decrease in Type III and IV cells that formed the PFR and PFF groups. Overall, PS TMNs were heterogeneous showing all four discharge types and the proportions of cells with specific discharge properties were different in the mutant.

Motor unit prediction in oculomotor nucleus and lack of changes in SOD1 ^{G93A} oculomotor motoneuron membrane properties

Given that mutant SOD1 is ubiquitously expressed we tested whether the observed changes in MN excitability based on MU type and MN discharge properties would also be present in the ALS-resistant oculomotor motoneurons of SOD1 ^{G93A} mutants of the same age range (P8–P12). Using the *k*-means clustering approach as before, we were able to classify two groups possibly corresponding to slow (PS) and fast (PF) MUs (Fig. 6*A*). Similar to TMNs, the PS OMNs had lower rheobase, higher-input resistance, and lower-membrane capacitance than PF cells in both WT and SOD1 ^{G93A} animals (also note *F*-ratios for the three categorical variables in Fig. 6, legend). The membrane properties of neither group were different in the SOD1 ^{G93A} OMNs compared with WT (Fig. 6*B*; Table 2). The proportions of PS and PF OMNs were also similar in WT and SOD1 ^{G93A} mice (Fig. 6*C*). The distribution of cells within the P8–P12 age group considered is given in Figure 6*D*. Qualitative differences were noted in the PS and PF *f–I* curves of WT and SOD1 ^{G93A} OMNs that may represent altered homeostasis of the underlying motor pools (Fig. 7). Particularly, the WT PS OMNs presented distinct bilinear *f–I* relationship that did not occur in the mutant PS OMNs over the range of current injections tested and the latter appears to be less excitable at lower values of current injection. Alternatively, the mutant PF OMNs appear to be more excitable than WT PF OMNs in a somewhat compensating manner (an example in Fig. 7*A*). However, there was no significant change in the steady-state *f–I* responses between WT and mutant OMNs among either predicted MU groups (two-way repeated-measures ANOVA). In summary, OMNs could be clustered into two distinct PS and PF motor unit types and neither groups presented significant alterations in membrane properties in the mutant mice compared with WT.

Discharge patterns of OMNs and lack of changes in the SOD1 ^{G93A} oculomotor nucleus

An examination of the discharge characteristics of OMNs in response to triangular ramp current injections revealed three types of discharge patterns (Fig. 8*A–C*). Type I corresponds to cells showing a linear *f–I* relationship on ascending and descending current ramps (Fig. 8*A*). Type II corresponds to "rate adapting" cells that show frequency adaptation during the descending ramp (Fig. 8*B*). Type III corresponds to the "sustained linear" pattern with an extended frequency range during the descending ramp below the firing threshold of the ascending ramp phase (Fig. 8*C*). All three patterns were found among SOD1 ^{G93A} OMNs as well. Moreover, there was no significant redistribution of the discharge types in the SOD1 ^{G93A} Mot III compared with WT (Fig. 8*D*) and we did not observe any subtype specific excitability changes. Additionally, the distribution of the discharge types was similar among PS and PF MU types (Fig. 8*E*) among WT and SOD1 ^{G93A} OMNs.

Jaw closer motor pool simulations and predicted force development

In summary, brainstem motoneurons including the trigeminal and oculomotor neurons presented here do not show hyperexcitability in the form of increased *f–I* gain at P8–P12. However, rheobase and the proportions of cells showing different discharge characteristics show complex changes in the ALS vulnerable TMNs but not in the ALS-resistant OMNs. Specifically, TMNs predicted to form fast MUs show reduced rheobase and PS TMNs with linear discharge patterns show increased rheobase and are increased in proportions. If such opposite changes were to occur in the input thresholds of slow and fast MNs in a jaw motor pool, we hypothesized that there could be alterations in MN recruitment and muscle force development early on. To test such a possibility and to predict changes in the muscle force development, we used a simple motor pool model of a jaw closer motor pool.

The simulation model was constructed based on similar models for spinal motor pools (Heckman and Binder, 1991) that allowed explicit parameterization of recruitment thresholds and steady-state *f–I* gains. The model enabled simulation of muscle isometric forces due to changes in TMN recruitment thresholds based on observed changes in rheobase values. For simplicity, we only represent slow and fast MNs and combine FR and FF as fast MNs to simulate SOD1^{G93A} changes in recruitment threshold values and further assume no changes in muscle properties in the mutant at this presymptomatic age.

A jaw closer masseter pool consisting of 100 TMNs was constructed to estimate normal (WT) and altered (SOD1^{G93A}) isometric forces. Briefly, each model MN was defined using six experimentally derived parameters including threshold recruitment current (I_{thresh}) and frequency (f_{thresh}), steady-state primary (G_1) and secondary (G_2) gains, primary to secondary transition current (I_{trans}), and frequency (f_{trans}) derived from our experimental data (see Materials and Methods for detailed definitions of terms). The MN and motor unit properties for every fifth MN are listed in Table 3.

Based on the observed *f–I* gain and rheobase values in WT and mutant TMNs, we simulated three scenarios as follows:

Simulation of standard motor pool behavior

(1) For the standard condition, the primary *f–I* gains were set as $G_1 = 0.1$ Hz/pA for all 100 neurons. The secondary *f–I* gain G_2 was set at 0.06 Hz/pA for the first 30 neurons representing the slow MUs, and at 0.05 Hz/pA for the remaining 70 neurons representing the fast MUs. These values approximate our experimental values. The resulting *f–I* curves for every 10th neu-

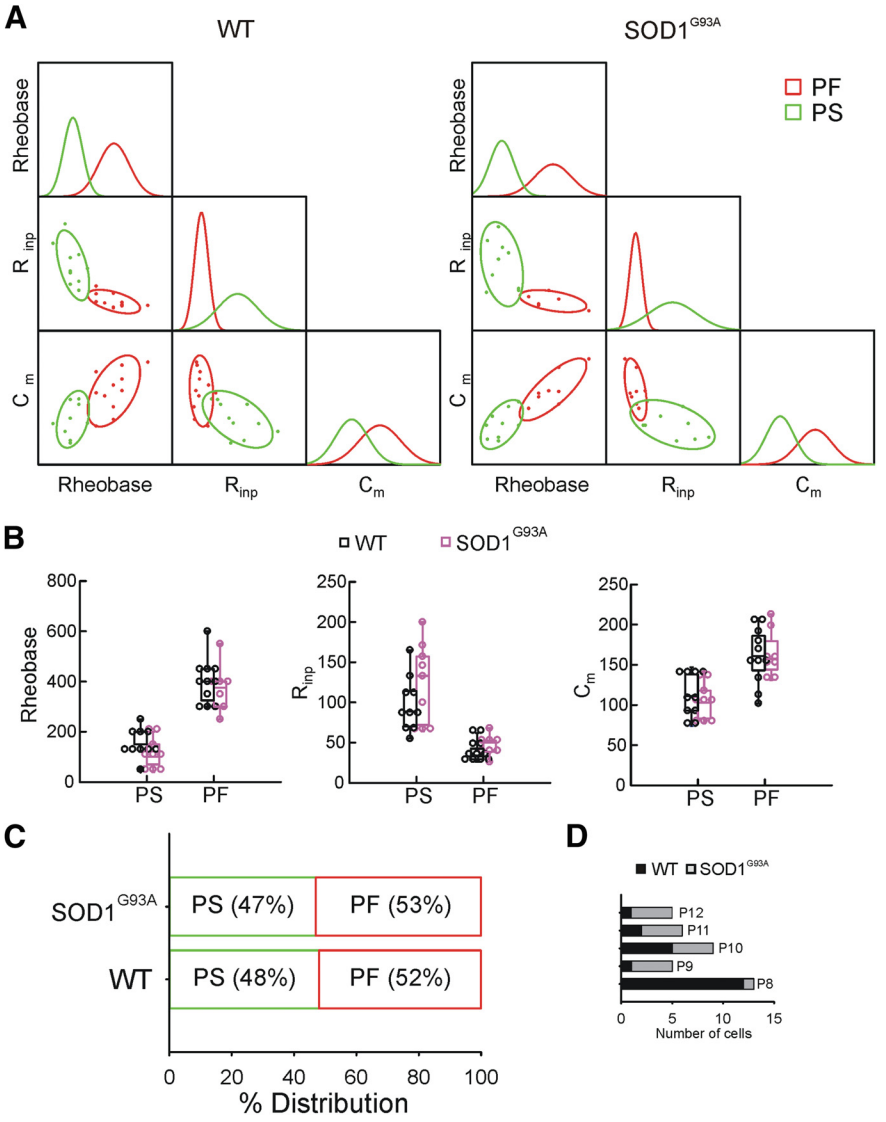

Figure 6. Motor unit classification based on OMN membrane properties. ***A***, Scatterplot matrices of membrane properties including rheobase, R_{inp} and C_m showing the result of *k*-means clustering based classification of motor units with PS in green and PF in red, in both WT (left) and SOD1^{G93A} (right) OMNs. The diagonal cells show the normal curves for each MU group. In WT the *F*-ratios were 52.7, 31.3, and 11.7, and in the mutant these values were 62.9, 17.9, and 21.5, respectively for rheobase, input resistance, and membrane capacitance. ***B***, Comparison of membrane properties of MU groups between WT (black) and SOD1^{G93A} (magenta) OMNs. No statistical differences were found. Error bars indicate SD. ***A***, ***B***, Units of rheobase, R_{inp} and C_m are pA, MΩ, and pF, respectively. ***C***, Percentage of cells classified as PS and PF units in WT and mutant groups. ***D***, Distribution of cells across the age range considered (P8–P12). Data from 14 WT mice ($n = 21$) and 12 SOD1^{G93A} mutant mice ($n = 17$), where *n* is the number of cells.

Table 2. Membrane properties of WT and SOD1^{G93A} OMNs classified by predicted MU type

	PS		PF	
Membrane property	WT ($n = 10$)	SOD1^{G93A} ($n = 9$)	WT ($n = 11$)	SOD1^{G93A} ($n = 8$)
C_m, pF	114.2 ± 8.6	105.1 ± 7.7	161.1 ± 10.4	163.3 ± 10.1
R_{inp}, MΩ	97.3 ± 10.6	123.5 ± 16.5	37.2 ± 3.5	47.0 ± 4.5
RMP, mV	−56.9 ± 1.8	−57.9 ± 1.3	−59.1 ± 1.2	−59.3 ± 1.0
Rheobase, pA	162.0 ± 17.3	113.9 ± 20.0	400.0 ± 27.0	368.8 ± 32.6
AP threshold, mV	−43.7 ± 1.9	−42.4 ± 2.0	−40.8 ± 1.7	−40.5 ± 1.4
AP height, mV	88 ± 3.6	87.6 ± 2.3	93.7 ± 1.8	92.0 ± 2.9
AP half-width, ms	0.9 ± 0.1	1.0 ± 0.1	0.7 ± 0.03	0.7 ± 0.04
AHP, mV	−4.7 ± 1.2	−7.2 ± 1.6	−2.8 ± 0.3	−2.6 ± 0.4

Values reported as mean ± SEM. Student *t* tests were performed for statistical comparison between WT and SOD1^{G93A} neurons within the two predicted MU types.

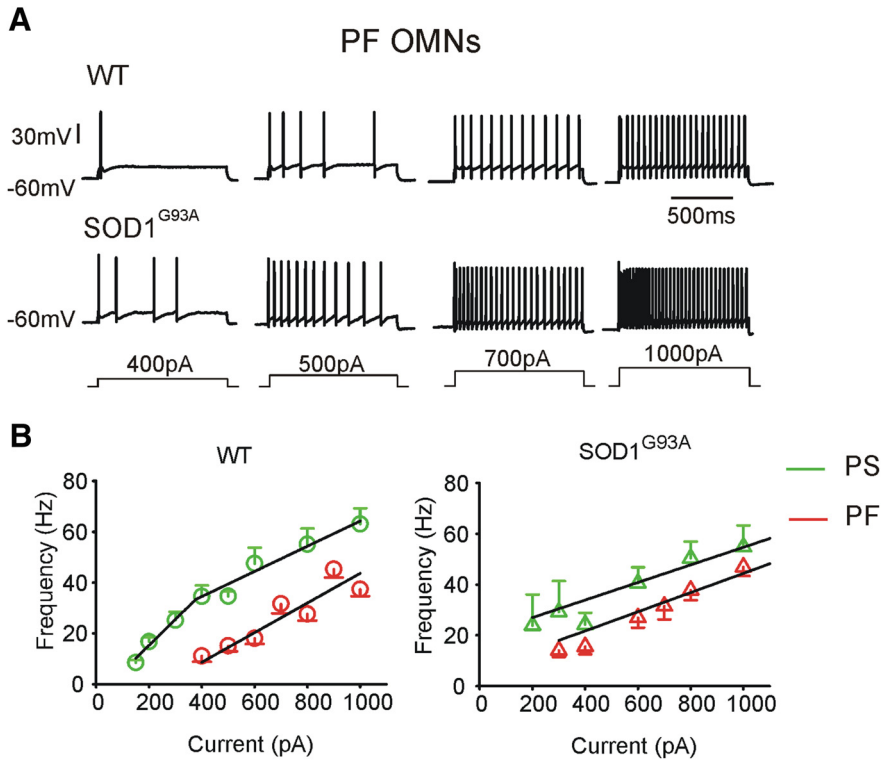

Figure 7. Frequency–current responses in the predicted OMN motor units. ***A***, Membrane voltage responses to increasing levels of 1 s current injection (bottom traces); top and bottom traces show example PF OMNs from WT and SOD1 ^{G93A} mice respectively. ***B***, Average steady-state frequency–current responses in WT (circles) and SOD1 ^{G93A} (triangles) OMNs. The PS (WT: $n = 9$ cells from 6 animals; SOD1 ^{G93A}: $n = 5$ cells from 4 animals) and PF cells (WT: 11 cells from 10 animals; SOD1 ^{G93A}: $n = 7$ cells from 6 animals) are depicted in green and red, respectively. Error bars indicate SEM, and black lines indicate linear fits to OMN frequencies. Among the respective MU groups, there were no statistically significant differences between WT and SOD1 ^{G93A} (two-way repeated-measures ANOVA).

ron are shown in Figure 9*A* (left). To generate I_{thresh} values for individual MNs, first we constructed a line with a certain slope and offset that resulted in a range of 100–950 pA from the first to the 100th neuron in the pool. This provided a ~10-fold range of I_{thresh} across the pool reflecting the rheobase range in our data. Each MN in the pool was assigned I_{thresh} value along this line with evenly spaced increase in I_{thresh} between consecutive model neurons (Fig. 9*A*, middle). The corresponding control isometric muscle force is shown in Figure 9*A* (right).

Simulation of recruitment threshold changes in SOD1 ^{G93A} TMNs

(2) We modeled the observed aberration in MN recruitment threshold of fast and slow SOD1 ^{G93A} TMNs in two steps. First, we compressed the I_{thresh} range of only the fast MNs to represent the observed reduced threshold for recruitment. We did so, by altering the I_{thresh}–MN line under standard conditions to a bilinear distribution of I_{thresh}. The I_{thresh} values of slow MUs remained unaltered, whereas those of the fast MNs were now sampled along a line with reduced slope resulting in a compression of I_{thresh} range across the fast MUs as shown by the red trace in Figure 9*B* (left). The resulting change in the muscle isometric force is shown by the red trace in Figure 9B (right). Note that reduced recruitment thresholds of large TMNs could profoundly enhance the steepness of the sigmoidal force curve. Finally, to model the concomitant I_{thresh} increases in slow MUs, we increased the slope of the lower arm of the I_{thresh}–MN line that resulted in an increase in the sampled I_{thresh} values for slow MU neurons (Fig. 9*B*, left, blue trace). Note that such reorganization of I_{thresh} values further simulates an increased proportion of low-threshold smaller neurons. This modification resulted in partial compensation of the isometric force as shown in Figure 9*B* (right, blue trace).

Simulation of f–I *gain changes*

(3) Because increased *f–I* gain has been noted in other ALS-vulnerable brainstem and spinal MNs we tested the potential effect of changes in *f–I* gains. We simulated opposite changes in *f–I* gains of fast and slow MU TMNs by increasing the gains of fast MU neurons and decreasing the gains of slow MU neurons as in Figure 9*C* (left). The corresponding isometric force is shown in Figure 9*C* (right). Note that the *f–I* gain changes produce a negligible effect on force development (compare green trace with the black control trace in the figure).

In Figure 9*D*, we show a comparison between the force deviations due to I_{thresh} and *f–I* gain changes detailed above. Note from the blue and green curves in Figure 9*D* that hypoexcitability in I_{thresh} of slow MU TMNs can suppress the initiation of force development. However, as input levels increase and larger forces develop, note the hypoexcitability in I_{thresh} of low-threshold TMNs compensates for the hyperexcitability of I_{thresh} in fast MU TMNs. Moreover *f–I* gain changes considered here resulted in negligible force deviation from standard condition. Finally, when both *f–I* gain changes and I_{thresh} changes were simultaneously simulated the resulting isometric force shows a reduction in the dynamic range of the motor pool input–output relationship (Fig. 9*E*). The distortion in the isometric force curve (Fig. 9*E*, orange) compared with control curve (Fig. 9*E*, black) highlights a change in the equilibrium of the motor pool function.

Discussion

A significant finding of this study shows that ALS-vulnerable SOD1 ^{G93A} MNs exhibit more complex changes in excitability than previously reported. Specifically, SOD1 ^{G93A} TMNs predicted to form fast MUs show a hyperexcitable shift in rheobase. However, a surprising observation was that a subset of predicted slow MU TMNs in SOD1 ^{G93A} cells with distinct discharge properties increased in proportions and showed a hypoexcitable shift in rheobase and voltage threshold for spike initiation. Such excitability changes were absent in the disease-resistant OMNs. The observed changes in SOD1 ^{G93A} TMNs are expected to alter motor unit recruitment and jaw muscle force development. To test this hypothesis, we constructed a simplified JC motor pool model using computer simulations. Model results suggest that hyperexcitable alterations in recruitment threshold of fast motor units would result in a steeper input–output relationship of the motor pool, suggesting more rapid muscle force development. Furthermore, such rapid force development can be partly compensated by the observed hypoexcitable shifts and increased slow motor unit composition in the mutants. Together these changes could reduce the dynamic range of motor pool input-

output function. Moreover, near low levels of pool inputs, hypoexcitability of slow TMNs can suppress force initiation.

Motor unit prediction and distribution of electrophysiological properties

Using *k*-means clustering approach we were able to successfully identify three clusters potentially corresponding to slow, fast fatigue resistant and fast fatigable TMNs and two clusters potentially corresponding to slow and fast OMNs. The *F*-ratio indicative of the power of the clustering variable was maximal for rheobase followed by input resistance and capacitance in TMNs consistent with the greater accuracy of MU prediction using rheobase as a discriminant variable in previous studies on spinal MNs (Fleshman et al., 1981; Zengel et al., 1985; but see Gardiner, 1993). A similar trend in *F*-ratio was also noted in OMN clustering, however, the input resistance was less powerful in MU prediction compared with TMNs.

Although the high-threshold MNs are unambiguously α-motoneurons that innervate the extrafusal muscles, some low-threshold MNs could be gamma MNs that innervate the muscle spindles. Parameters that may distinguish gamma MNs from α MNs, such as higher antidromic stimulation threshold (*in vivo*) or lack of monosynaptic responses during afferent stimulation (Sessle, 1977) are both not feasible and definitive methods to use in the neonatal *in vitro* brain slice preparation. Although we have previously demonstrated stimulation techniques in brain slices to study the physiology and pharmacology of synaptic inputs from the sensory mesencephalic nucleus to TMNs (Trueblood et al., 1996; Del Negro and Chandler, 1998), many of these connections are lost during brain-slice preparation and cannot be used as a reliable approach to test the lack of afferent connections to segregate gamma TMNs. Furthermore, gamma TMNs are spontaneously active *in vivo* (Sessle, 1977) and we did not encounter such MNs in our *in vitro* dataset.

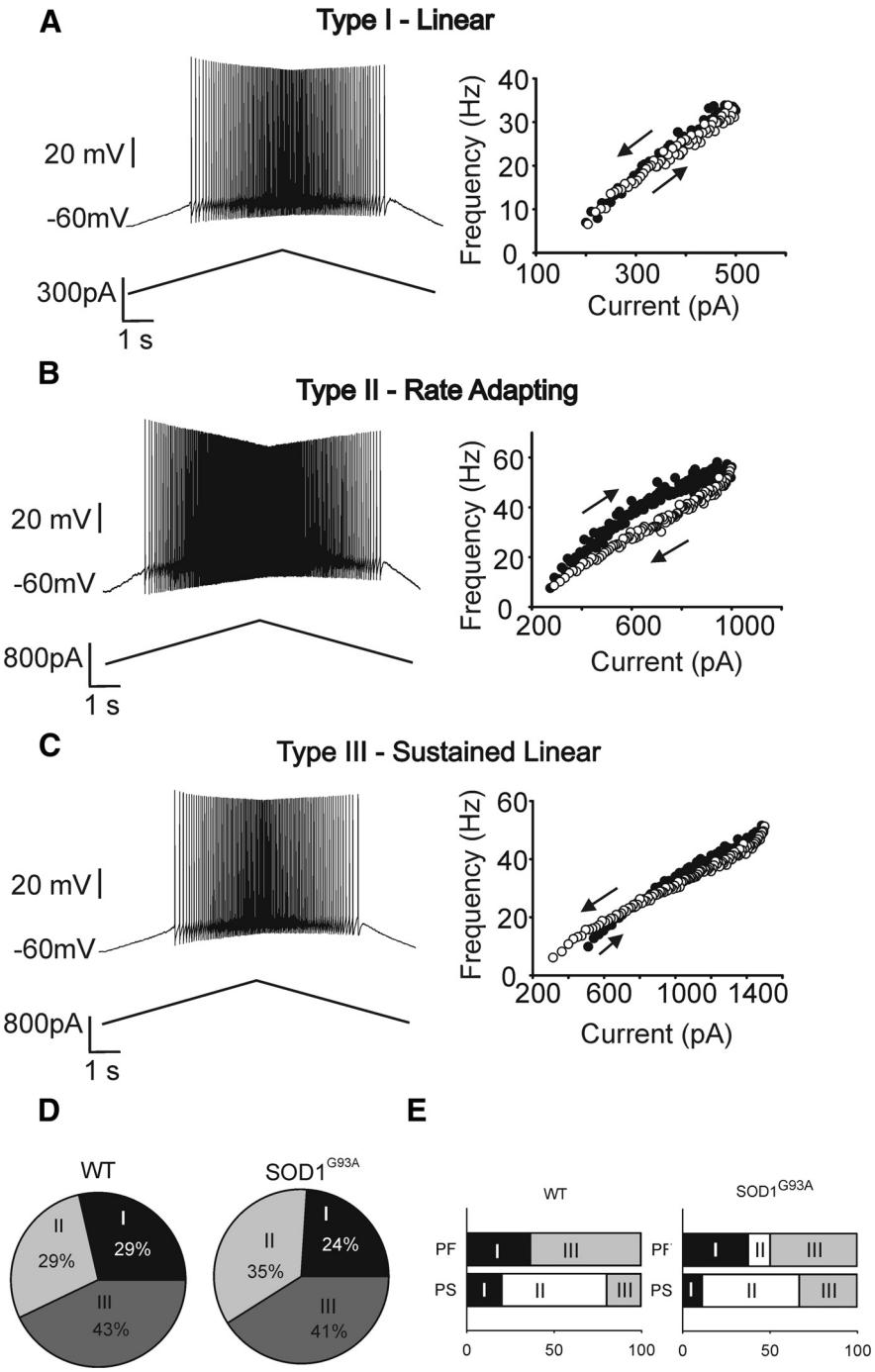

Figure 8. Discharge patterns of OMNs. ***A–C***, Membrane voltage responses (left) of three OMNs to injection of triangular ramp currents (bottom traces) and the corresponding plots of instantaneous discharge frequency responses to ascending and descending current ramps (right) are shown by filled and open circles respectively. Arrows point to the direction of current ramp. Types I–III refer to the three types of discharge patterns (see text). ***D***, Proportions of the three types of discharge patterns found in WT and SOD1^{G93A} OMNs were similar and not statistically different (χ^2 proportionality test). ***E***, Horizontal bar charts show percentage distribution of the three discharge types among PS and PF OMNs.

Assumptions and limitations of motor pool simulation model

First, we assume that our TMN dataset predominantly represents the JC motor pool(s) neurons because the TMNs filled with the red dye (AlexaFluor 568) during patch-clamp recording were identified *post hoc* in the dorsolateral Mot V where JC MNs are localized (Mizuno et al., 1975). Second, we use membrane properties including rheobase and input resistance that are suggested to predict MU types with >90% accuracy (Zengel et al., 1985). We further directly extrapolate the MN recruitment threshold and *f–I* gains found in this dataset into a single JC motor pool model. Nonetheless, due to the simplified representation of each model MN based on experimentally derived properties (see Materials and Methods, and Results), the insight from the model simulations that rheobase change would have a profound effect on steady-state motor pool input–output relationship should be reasonable. However, more de-

Table 3. Simulated jaw motor unit properties

	Motoneuron properties												
	WT	MUT	WT	MUT	WT	MUT	WT	MUT			Muscle properties		
MN	I_{thresh} (pA)	I_{thresh} (pA)	I_{trans} (pA)	I_{trans} (pA)	G_1 (Hz/pA)	G_1 (Hz/pA)	G_2 (Hz/pA)	G_2 (Hz/pA)	f_{thresh} (Hz)	f_{trans} (Hz)	F_{max} (M)	T_f	p
5	142.5	140.0	206.1	203.6	0.1	0.03	0.06	0.06	6.4	20.4	0.013	17.1	2.7
10	185.0	200.0	248.6	263.6	0.1	0.03	0.06	0.06	6.9	20.9	0.023	17.65	2.8
15	227.5	260.0	291.1	323.6	0.1	0.03	0.06	0.06	7.4	21.4	0.033	18.19	2.9
20	270.0	320.0	333.6	383.6	0.1	0.03	0.06	0.06	7.9	21.9	0.043	18.74	3.1
25	312.5	380.0	376.1	443.6	0.1	0.03	0.06	0.06	8.4	22.4	0.053	19.28	3.2
30	355.0	440.0	418.6	503.6	0.1	0.03	0.06	0.06	8.9	22.9	0.063	19.81	3.3
35	397.5	466.3	461.1	529.9	0.1	0.15	0.05	0.03	9.4	23.4	0.073	20.34	3.4
40	440.0	490.0	503.6	553.6	0.1	0.15	0.05	0.03	9.9	23.9	0.083	20.88	3.5
45	482.5	513.8	546.1	577.4	0.1	0.15	0.05	0.03	10.4	24.4	0.093	21.4	3.6
50	525.0	537.5	588.6	601.1	0.1	0.15	0.05	0.03	10.9	24.9	0.103	21.93	3.7
55	567.5	561.3	631.1	624.9	0.1	0.15	0.05	0.03	11.4	25.4	0.113	22.45	3.9
60	610.0	585.0	673.6	648.6	0.1	0.15	0.05	0.03	11.9	25.9	0.123	22.98	4
65	652.5	608.8	716.1	672.4	0.1	0.15	0.05	0.03	12.4	26.4	0.133	23.5	4.1
70	695.0	632.5	758.6	696.1	0.1	0.15	0.05	0.03	12.9	26.9	0.143	24.02	4.2
75	737.5	656.3	801.1	719.9	0.1	0.15	0.05	0.03	13.4	27.4	0.153	24.54	4.3
80	780.0	680.0	843.6	743.6	0.1	0.15	0.05	0.03	13.9	27.9	0.163	25.06	4.4
85	822.5	703.8	886.1	767.4	0.1	0.15	0.05	0.03	14.4	28.4	0.173	25.57	4.5
90	865.0	727.5	928.6	791.1	0.1	0.15	0.05	0.03	14.9	28.9	0.183	26.09	4.7
95	907.5	751.3	971.1	814.9	0.1	0.15	0.05	0.03	15.4	29.4	0.193	26.61	4.8
100	950.0	775.0	1014	838.6	0.1	0.15	0.05	0.03	15.9	29.9	0.203	27.12	4.9

The model parameters are shown for every fifth cell in a pool of 100 MNs.

tailed MN models are essential to examine the effect of alterations in MN discharge patterns on motor pool behavior. Last, we assume no aberrations in the muscle fiber properties in the mutant compared with WT that requires empirical validation.

Discharge patterns of TMNs and OMNs

Similar to spinal MNs (Bennett et al., 2001a; Button et al., 2006; Turkin et al., 2010), we found that the brainstem TMNs and OMNs also displayed heterogeneous discharge patterns in response to triangular ramp current injections. However, the OMNs were somewhat less heterogeneous. Specifically, all four discharge patterns described for spinal MNs were present among TMNs, whereas only three types of patterns were present among OMNs. In comparison with discharge patterns observed in TMNs, Type I OMNs were qualitatively similar. However, Type II OMNs showed lesser degree of rate adaptation than TMNs. For example, for the Type II OMN shown in Figure 7*B*, the firing frequencies during descending ramp gradually merge with the ascending frequencies, thus abolishing the rate adaptation near recruitment frequency. Among Type III OMNs often an initial phase of rate adaptation was observed during the descending current ramp followed by a crossover of frequencies resulting in sustained firing. Such frequency crossover was not observed in TMNs. Type IV cells with a sustained hysteretic pattern were not observed among OMNs. Interestingly there was a significant change in the proportion of cells displaying the different discharge patterns in TMNs compared with OMNs in the SOD1^{G93A} animals. This suggests an altered homeostasis in the excitability of the vulnerable Mot V.

Effect of development on MN membrane properties

Based on *in vitro* studies, membrane properties of motoneurons change during the postnatal period (for review, see Carrascal et al., 2005). Moreover, among brainstem motoneurons, some membrane properties show opposite changes between different brainstem motor nuclei. For example, rheobase is suggested to decrease with postnatal age in oculomotor neurons (Carrascal et al., 2006), whereas it increases with postnatal age in hypoglossal neurons (Núñez-Abades et al., 1993). We show that the two types of postnatal age-matched motoneurons (TMNs and OMNs) present fundamental differences in the membrane properties in the mutant compared with WT. The cells were proportionately distributed across ages considered (P8–P12) in both genotypes for TMNs (Fig. 2*D*). For OMNs, we noted a slight bias toward P8 among WT and toward P12 in SOD1^{G93A}. Although this was a random occurrence, we further note that this did not lead to manifestation of age-related differences between WT and SOD1^{G93A} groups because we did not observe significant changes in any of the measured membrane properties between the two groups among either of the predicted MU types. Moreover, developmental changes in OMN membrane properties are more dramatic at P0–P5, whereas such changes are not significant between P6–P10 and P11–P15 (Carrascal et al., 2006). Together, our results on ALS-vulnerable TMNs clearly demonstrate motor unit specific modifications in the mutant motoneurons, whereas the ALS-resistant mutant OMNs do not present such changes in the postnatal age range tested.

Possible mechanisms underlying MN excitability changes

Spinal MNs with sustained discharge patterns showed large persistent inward sodium and calcium currents (PICs) activated by supraspinal monoaminergic inputs. These PICs are modulated following spinal trauma and in ALS (Li and Bennett, 2003; Quinlan et al., 2011). Alternatively, MNs with linear discharge patterns are likely to have negligible PICs (Bennett et al., 2001a; Li et al., 2004). The fact that these two types of discharge patterns showed opposite changes in proportion and excitability in TMNs suggests that PICs play an integral role in the homeostatic regulation of MN and motor pool excitability (Elbasiouny et al., 2010; Martin et al., 2013). Recently we reported evidence for *tonic* GABAergic currents that can modulate TMN excitability and

their downregulation in SOD1^{G93A} TMNs (Venugopal and Chandler, 2012). Such reductions in tonic inhibition may underlie the reduced firing threshold in large TMNs. Alterations in potassium (Wainger et al., 2014) and persistent sodium conductance (Kuo et al., 2005; Bellingham, 2013) may also play a role. Concomitant opposite changes in large versus small TMN excitability highlights the existence of mechanisms coupling the excitability of different MNs within a motor pool. Noncell autonomous changes in astrocytes could play a role in such coupling (Bataveljić et al., 2012).

Role for intrinsic MN excitability changes in ALS pathogenesis

Motoneuron hyperexcitability has been widely reported in ALS patients (Vucic and Kiernan, 2006) and in animal and cell culture models (Pieri et al., 2003; Kuo et al., 2004; Durand et al., 2006; van Zundert et al., 2008; Quinlan et al., 2011; Wainger et al., 2014). Presymptomatically, hyperexcitability could make MNs hyperresponsive to glutamatergic inputs in turn leading to excessive intracellular calcium causing ER stress and triggering apoptotic cascade through mitochondrial overload (Grosskreutz et al., 2010; van Zundert et al., 2012). Therefore, factors reducing hyperexcitability are considered potential therapeutic targets. However, if we consider our results, it is clear that hypoexcitability concomitantly occurs in a distinct population of low-threshold TMNs with distinct discharge properties compared with the high-threshold cells that show hyperexcitable shifts. Within a homogeneous motor pool, hypoexcitability in low-threshold motoneurons can restrict/suppress muscle activation as shown by the model. Indeed, inhibiting MN excitability presymptomatically has been shown to induce pathological cellular responses and enhanced compensatory responses, whereas enhancing excitability was neuroprotective (Saxena et al., 2013).Together with the additional findings that hyperexcitability is not observed in adult mutant mice (Delestrée et al., 2014), it appears that a change toward hypoexcitability may indeed represent the disease process, whereas early hyperexcitability may represent a compensation. Therefore, identifying the distinct cellular and molecular properties of cells displaying reduced excitability in addition to hyperexcitability would serve as opportunistic targets for investigation into the underlying mechanisms contributing to disease progression.

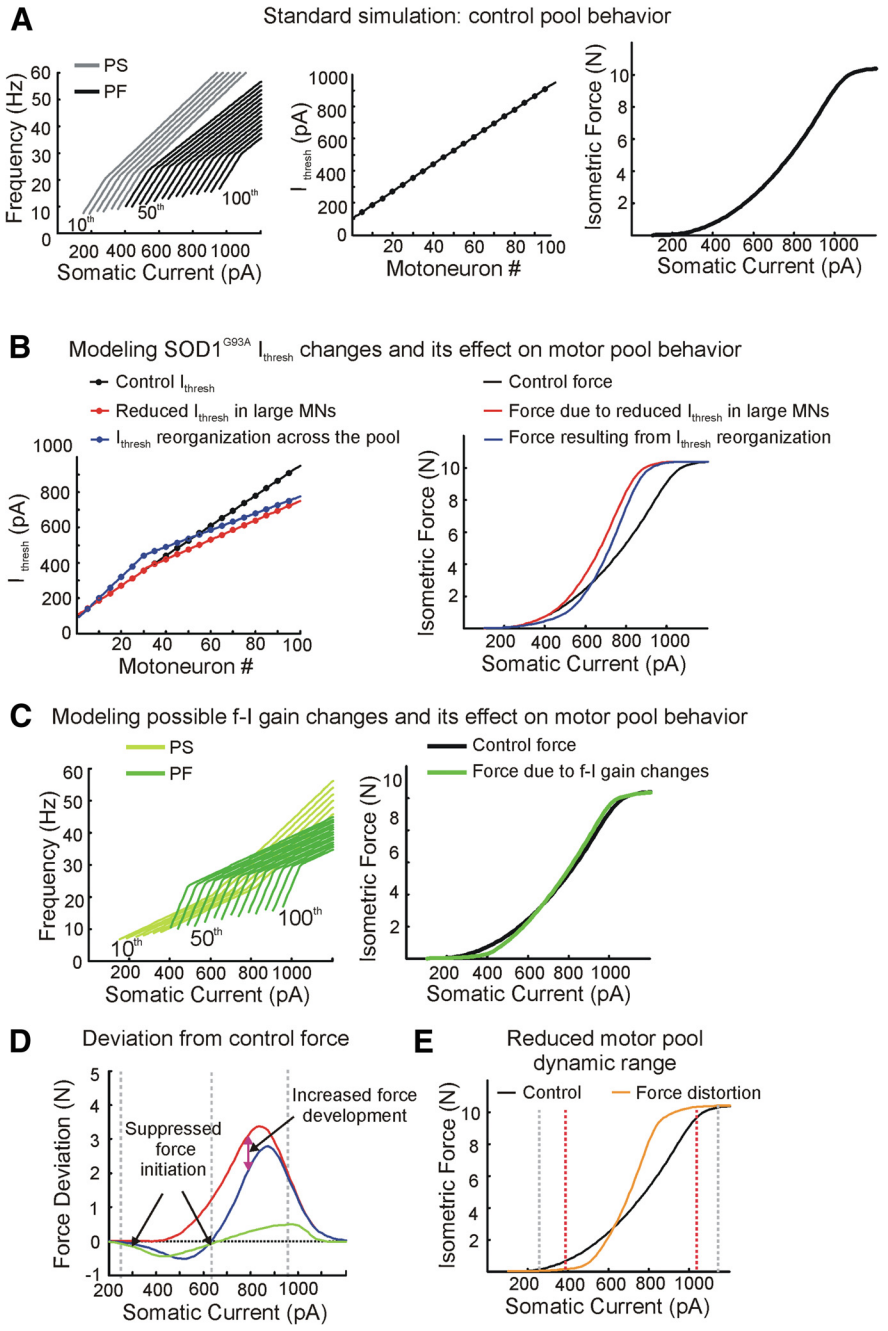

Figure 9. Simulation of effects of recruitment and *f–I* gain changes on JC motor pool behavior. ***A***, Standard/control condition. Left, Frequency– current curves shown for every 10th model MN with PS MNs represented in gray and PF MNs in black. Middle, An evenly spaced increasing distribution of I_{thresh} across the motor pool. Right, Resultant isometric force shown as a function of neural excitation (somatic current). ***B***, Left, Posited shifts in the distribution of I_{thresh} across the pool in the mutant TMNs. In red is shown the modeled reduction in rheobase of PF MNs obtained by a reduction in the slope of the linear I_{thresh} distribution of the 31st–100th cell. The blue trace shows a steeper distribution of I_{thresh} for PS MNs (1st–30th cell) reflecting an increase in rheobase values of these cells and reduced slope of I_{thresh} distribution of 31st–100th cell representing the reduced rheobase among PF MNs. Right, The corresponding alteration in the isometric muscle force is shown in red and blue, respectively, together with the standard force (black). ***C***, Effect of *f–I* gain changes on motor pool behavior. Left, Modified *f–I* curves shown for every 10th model MN with PS MNs represented in light green and PF MNs in dark green. Right, The corresponding alteration in the isometric muscle force is shown (green) together with the standard force (black). ***D***, Force deviations from control condition are shown with: (1) only *f–I* gain changes in green, (2) only I_{thresh} changes only among PF MNs in red, and (3) only I_{thresh} changes in both PF and PS MNs in blue. Dashed vertical lines highlight two regions: a left region showing deviations <0 for blue trace suggesting suppression of force initiation due to hypoexcitability, a right region showing deviations >0 for blue trace suggesting compensatory effect to limit PF TMN hyperexcitability. The green trace shows force deviation due to *f–I* gain changes. ***E***, Overall distortion in the isometric force due to both I_{thresh} and *f–I* gain changes is shown in orange together with the standard force in black. The region between red vertical lines shows reduced motor pool dynamic range compared with the region between gray vertical lines for control simulation.

References

Angenstein F, Niessen HG, Goldschmidt J, Vielhaber S, Ludolph AC, Scheich H (2004) Age-dependent changes in MRI of motor brain stem nuclei in a mouse model of ALS. Neuroreport 15:2271–2274. CrossRef Medline

Bataveljić D, Nikolić L, Milosević M, Todorović N, Andjus PR (2012) Changes in the astrocytic aquaporin-4 and inwardly rectifying potassium channel expression in the brain of the amyotrophic lateral sclerosis SOD1(G93A) rat model. Glia 60:1991–2003. CrossRef Medline

Bellingham MC (2013) Pre- and postsynaptic mechanisms underlying inhibition of hypoglossal motor neuron excitability by riluzole. J Neurophysiol 110:1047–1061. CrossRef Medline

Bennett DJ, Li Y, Siu M (2001a) Plateau potentials in sacrocaudal motoneurons of chronic spinal rats, recorded in vitro. J Neurophysiol 86:1955–1971. Medline

Bennett DJ, Li Y, Harvey PJ, Gorassini M (2001b) Evidence for plateau potentials in tail motoneurons of awake chronic spinal rats with spasticity. J Neurophysiol 86:1972–1982. Medline

Bories C, Amendola J, Lamotte d'Incamps B, Durand J (2007) Early electrophysiological abnormalities in lumbar motoneurons in a transgenic mouse model of amyotrophic lateral sclerosis. Eur J Neurosci 25:451–459. CrossRef Medline

Brooks BR (1996) Natural history of ALS: symptoms, strength, pulmonary function, and disability. Neurology 47:S71–81; discussion S81–82. CrossRef Medline

Bruijn LI, Miller TM, Cleveland DW (2004) Unraveling the mechanisms involved in motor neuron degeneration in ALS. Annu Rev Neurosci 27:723–749. CrossRef Medline

Burke RE (1981) Motor units: anatomy, physiology and functional organization. In: Handbook of physiology: the nervous system, motor control, pp 877–994. Bethesda, MD: American Physiological Society.

Button DC, Gardiner K, Marqueste T, Gardiner PF (2006) Frequency-current relationships of rat hindlimb alpha-motoneurones. J Physiol 573:663–677. CrossRef Medline

Carrascal L, Nieto-Gonzalez JL, Cameron WE, Torres B, Nunez-Abades PA (2005) Changes during the postnatal development in physiological and anatomical characteristics of rat motoneurons studied in vitro. Brain Res Rev 49:377–387. CrossRef Medline

Carrascal L, Nieto-Gonzalez JL, Núñez-Abades P, Torres B (2006) Temporal sequence of changes of electrophysiological properties of oculomotor neurons during postnatal development. Neuroscience 140:1223–1237. CrossRef Medline

Chandler SH, Hsaio CF, Inoue T, Goldberg LJ (1994) Electrophysiological properties of guinea pig trigeminal motoneurons recorded in vitro. J Neurophysiol 71:129–145. Medline

Cotel F, Antri M, Barthe JY, Orsal D (2009) Identified ankle extensor and flexor motoneurons display different firing profiles in the neonatal rat. J Neurosci 29:2748–2753. CrossRef Medline

Del Negro CA, Chandler SH (1998) Regulation of intrinsic and synaptic properties of neonatal rat trigeminal motoneurons by metabotropic glutamate receptors. J Neurosci 18:9216–9226. Medline

del Negro CA, Hsiao CF, Chandler SH (1999) Outward currents influencing bursting dynamics in guinea pig trigeminal motoneurons. J Neurophysiol 81:1478–1485. Medline

Delestrée N, Manuel M, Iglesias C, Elbasiouny SM, Heckman CJ, Zytnicki D (2014) Adult motoneurons are not hyperexcitable in a mouse model of inherited amyotrophic lateral sclerosis. J Physiol 592:1687–1703. CrossRef Medline

Durand J, Amendola J, Bories C, Lamotte d'Incamps B (2006) Early abnormalities in transgenic mouse models of amyotrophic lateral sclerosis. J Physiol Paris 99:211–220. CrossRef Medline

Elbasiouny SM, Amendola J, Durand J, Heckman CJ (2010) Evidence from computer simulations for alterations in the membrane biophysical properties and dendritic processing of synaptic inputs in mutant superoxide dismutase-1 motoneurons. J Neurosci 30:5544–5558. CrossRef Medline

Enoka RM, Pearson KG (2013) The motor unit and muscle action. In: Principles of neural science, Ed 5 (Kandel ER, Schwartz JH, Jessell TM, Seigelbaum SA, Hudspeth AJ, eds), pp 768–788. New York: McGraw-Hill.

Ferrucci M, Spalloni A, Bartalucci A, Cantafora E, Fulceri F, Nutini M, Longone P, Paparelli A, Fornai F (2010) A systematic study of brainstem motor nuclei in a mouse model of ALS, the effects of lithium. Neurobiol Dis 37:370–383. CrossRef Medline

Fleshman JW, Munson JB, Sypert GW, Friedman WA (1981) Rheobase, input resistance, and motor-unit type in medial gastrocnemius motoneurons in the cat. J Neurophysiol 46:1326–1338. Medline

Gardiner PF (1993) Physiological properties of motoneurons innervating different muscle unit types in rat gastrocnemius. J Neurophysiol 69:1160–1170. Medline

Gojo K, Abe S, Ide Y (2002) Characteristics of myofibres in the masseter muscle of mice during postnatal growth period. Anat Histol Embryol 31:105–112. CrossRef Medline

Gordon T, Tyreman N, Li S, Putman CT, Hegedus J (2010) Functional overload saves motor units in the SOD1–G93A transgenic mouse model of amyotrophic lateral sclerosis. Neurobiol Dis 37:412–422. CrossRef Medline

Granit R, Kernell D, Lamarre Y (1966) Algebraical summation in synaptic activation of motoneurones firing within the "primary range" to injected currents. J Physiol 187:379–399. Medline

Grosskreutz J, Van Den Bosch L, Keller BU (2010) Calcium dysregulation in amyotrophic lateral sclerosis. Cell Calcium 47:165–174. CrossRef Medline

Gupta A, Elgammal FS, Proddutur A, Shah S, Santhakumar V (2012) Decrease in tonic inhibition contributes to increase in dentate semilunar granule cell excitability after brain injury. J Neurosci 32:2523–2537. CrossRef Medline

Gurney ME, Pu H, Chiu AY, Dal Canto MC, Polchow CY, Alexander DD, Caliendo J, Hentati A, Kwon YW, Deng HX, et al. (1994) Motor neuron degeneration in mice that express a human Cu, Zn superoxide dismutase mutation. Science 264:1772–1775. CrossRef Medline

Heckman CJ, Binder MD (1991) Computer simulation of the steady-state input-output function of the cat medial gastrocnemius motoneuron pool. J Neurophysiol 65:952–967. Medline

Hegedus J, Putman CT, Gordon T (2007) Time course of preferential motor unit loss in the SOD1 G93A mouse model of amyotrophic lateral sclerosis. Neurobiol Dis 28:154–164. CrossRef Medline

Hegedus J, Putman CT, Tyreman N, Gordon T (2008) Preferential motor unit loss in the SOD1 G93A transgenic mouse model of amyotrophic lateral sclerosis. J Physiol 586:3337–3351. CrossRef Medline

Hiiemae K (1971) The structure and function of the jaw muscles in the rat: II. Fibre type and composition. Zool J Linn 50:101–109. CrossRef

Kanning KC, Kaplan A, Henderson CE (2010) Motor neuron diversity in development and disease. Ann Rev Neurosci 33:409–440. CrossRef Medline

Kernell D (1966) Input resistance, electrical excitability, and size of ventral horn cells in cat spinal cord. Science 152:1637–1640. CrossRef Medline

Kernell D (1979) Rhythmic properties of motoneurones innervating muscle fibres of different speed in m. gastrocnemius medialis of the cat. Brain Res 160:159–162. CrossRef Medline

Kernell D, Eerbeek O, Verhey BA (1983) Relation between isometric force and stimulus rate in cat's hindlimb motor units of different twitch contraction time. Exp Brain Res 50:220–227. Medline

Kuo JJ, Schonewille M, Siddique T, Schults AN, Fu R, Bär PR, Anelli R, Heckman CJ, Kroese AB (2004) Hyperexcitability of cultured spinal motoneurons from presymptomatic ALS mice. J Neurophysiol 91:571–575. CrossRef Medline

Kuo JJ, Siddique T, Fu R, Heckman CJ (2005) Increased persistent Na(+) current and its effect on excitability in motoneurones cultured from mutant SOD1 mice. J Physiol 563:843–854. CrossRef Medline

Li Y, Bennett DJ (2003) Persistent sodium and calcium currents cause plateau potentials in motoneurons of chronic spinal rats. J Neurophysiol 90:857–869. CrossRef Medline

Li Y, Gorassini MA, Bennett DJ (2004) Role of persistent sodium and calcium currents in motoneuron firing and spasticity in chronic spinal rats. J Neurophysiol 91:767–783. CrossRef Medline

Limwongse V, DeSantis M (1977) Cell body locations and axonal pathways of neurons innervating muscles of mastication in the rat. Am J Anat 149:477–488. CrossRef Medline

Martin E, Cazenave W, Cattaert D, Branchereau P (2013) Embryonic alteration of motoneuron morphology induces hyperexcitability in the mouse model of amyotrophic lateral sclerosis. Neurobiol Dis 54:116–126. CrossRef Medline

Matsuda K, Uemura M, Kume M, Matsushima R, Mizuno N (1978) Topographical representation of masticatory muscles in the motor trigeminal nucleus in the rabbit: a HRP study. Neurosci Lett 8:1–4. CrossRef Medline

Mizuno N, Konishi A, Sato M (1975) Localization of masticatory motoneurons in the cat and rat by means of retrograde axonal transport of horseradish peroxidase. J Comp Neurol 164:105–115. CrossRef Medline

Niessen HG, Angenstein F, Sander K, Kunz WS, Teuchert M, Ludolph AC, Heinze HJ, Scheich H, Vielhaber S (2006) In vivo quantification of spinal and bulbar motor neuron degeneration in the G93A-SOD1 transgenic mouse model of ALS by T2 relaxation time and apparent diffusion coefficient. Exp Neurol 201:293–300. CrossRef Medline

Nimchinsky EA, Young WG, Yeung G, Shah RA, Gordon JW, Bloom FE, Morrison JH, Hof PR (2000) Differential vulnerability of oculomotor, facial, and hypoglossal nuclei in G86R superoxide dismutase transgenic mice. J Comp Neurol 416:112–125. CrossRef Medline

Núñez-Abades PA, Spielmann JM, Barrionuevo G, Cameron WE (1993) In vitro electrophysiology of developing genioglossal motoneuronsin the rat. J Neurophysiol 70:1401–1411. Medline

Pieri M, Albo F, Gaetti C, Spalloni A, Bengtson CP, Longone P, Cavalcanti S, Zona C (2003) Altered excitability of motor neurons in a transgenic mouse model of familial amyotrophic lateral sclerosis. Neurosci Lett 351: 153–156. CrossRef Medline

Pun S, Santos AF, Saxena S, Xu L, Caroni P (2006) Selective vulnerability and pruning of phasic motoneuron axons in motoneuron disease alleviated by CNTF. Nat Neurosci 9:408–419. CrossRef Medline

Quinlan KA, Schuster JE, Fu R, Siddique T, Heckman CJ (2011) Altered postnatal maturation of electrical properties in spinal motoneurons in a mouse model of amyotrophic lateral sclerosis. J Physiol 589:2245–2260. CrossRef Medline

Radcliffe CB, Lockhart Clarke J (1862) An important case of paralysis and muscular atrophy with disease of the nervous centers. Br Foreign Med Chir Rev 30.

Saxena S, Roselli F, Singh K, Leptien K, Julien JP, Gros-Louis F, Caroni P (2013) Neuroprotection through excitability and mTOR required in ALS motoneurons to delay disease and extend survival. Neuron 80:80–96. CrossRef Medline

Schurr A, West CA, Rigor BM (1988) Lactate-supported synaptic function in the rat hippocampal slice preparation. Science 240:1326–1328. CrossRef Medline

Sessle BJ (1977) Identification of alpha and gamma trigeminal motoneurons and effects of stimulation of amygdala, cerebellum, and cerebral cortex. Exp Neurol 54:303–322. CrossRef Medline

Taylor A, Cody FW, Bosley MA (1973) Histochemical and mechanical properties of the jaw muscles of the cat. Exp Neurol 38:99–109. CrossRef Medline

Trueblood PR, Levine MS, Chandler SH (1996) Dual-component excitatory amino acid-mediated responses in trigeminal motoneurons and their modulation by serotonin in vitro. J Neurophysiol 76:2461–2473. Medline

Turkawski SJ, van Eijden TM (2000) EMG power spectrum and motor unit characteristics in the masseter muscle of the rabbit. J Dent Res 79:950–956. CrossRef Medline

Turkin VV, O'Neill D, Jung R, Iarkov A, Hamm TM (2010) Characteristics and organization of discharge properties in rat hindlimb motoneurons. J Neurophysiol 104:1549–1565. CrossRef Medline

Uemura-Sumi M, Takahashi O, Matsushima R, Takata M, Yasui Y, Mizuno N (1982) Localization of masticatory motoneurons in the trigeminal motor nucleus of the guinea pig. Neurosci Lett 29:219–224. CrossRef Medline

van Eijden TM, Turkawski SJ (2002) Action potentials and twitch forces of rabbit masseter motor units at optimum jaw angle. Arch Oral Biol 47: 607–612. CrossRef Medline

van Zundert B, Peuscher MH, Hynynen M, Chen A, Neve RL, Brown RH Jr, Constantine-Paton M, Bellingham MC (2008) Neonatal neuronal circuitry shows hyperexcitable disturbance in a mouse model of the adult-onset neurodegenerative disease amyotrophic lateral sclerosis. J Neurosci 28:10864–10874. CrossRef Medline

van Zundert B, Izaurieta P, Fritz E, Alvarez FJ (2012) Early pathogenesis in the adult-onset neurodegenerative disease amyotrophic lateral sclerosis. J Cell Biochem 113:3301–3312. CrossRef Medline

Venugopal S, Chandler SH (2012) Early evidence for disruption of cellular homeostasis in a mouse model for neurodegenerative motoneuron disease. In: Annual Society for Neuroscience Meeting: New Orleans, LA.

Vucic S, Kiernan MC (2006) Axonal excitability properties in amyotrophic lateral sclerosis. Clin Neurophysiol 117:1458–1466. CrossRef Medline

Wainger BJ, Kiskinis E, Mellin C, Wiskow O, Han SS, Sandoe J, Perez NP, Williams LA, Lee S, Boulting G, Berry JD, Brown RH Jr, Cudkowicz ME, Bean BP, Eggan K, Woolf CJ (2014) Intrinsic membrane hyperexcitability of amyotrophic lateral sclerosis patient-derived motor neurons. Cell Reports 7:1–11. CrossRef Medline

Zengel JE, Reid SA, Sypert GW, Munson JB (1985) Membrane electrical properties and prediction of motor-unit type of medial gastrocnemius motoneurons in the cat. J Neurophysiol 53:1323–1344. Medline